Lehrstuhl für Bildverarbeitung
Institute of Imaging & Computer Vision

Defect Interpolation in Digital Radiography - How Object-Oriented Transform Coding Helps

Til Aach and Volker Metzler

in: SPIE Vol. 4322: Medical Imaging 2001. See also BIBTEX entry below.

BIBTEX:

```
@inproceedings{AAC01a,
author = {Til Aach and Volker Metzler},
title = {Defect Interpolation in Digital Radiography - How Object-Oriented
                        Transform Coding Helps},
booktitle = {SPIE Vol. 4322: Medical Imaging 2001},
editor = {M. Sonka and K. M. Hanson},
publisher = {SPIE},
address = {San Diego, USA},
month = {February 17--22},
year = {2001},
pages = {824--835}}
```


document created on: December 15, 2006
created from file: spiemi01coverpage.tex
cover page automatically created with CoverPage.sty
(available at your favourite CTAN mirror)

RWTH AACHEN
RHEINISCH-WESTFÄLISCHE TECHNISCHE HOCHSCHULE AACHEN

Defect Interpolation in Digital Radiography — How Object-Oriented Transform Coding Helps

Til Aach, Volker Metzler

Institute for Signal Processing, Medical University of Lübeck
Ratzeburger Allee 160, D-23538 Lübeck, Germany

ABSTRACT

Today's solid state flat panel radiography detectors provide images which contain artifacts caused by lines, columns and clusters of inactive pixels. If not too large, such defects can be filled by interpolation algorithms which usually work in the spatial domain. This paper describes an alternative spectral domain approach to defect interpolation. The acquired radiograph is modelled as the undistorted image multiplied by a known binary defect window. The window effect is then removed by deconvolving the window spectrum from the spectrum of the observed, distorted radiograph. The basic ingredient of our interpolation algorithm is an earlier approach to block transform coding of arbitrarily shaped image segments, that extrapolates the segment internal intensities over a block into which the segment is embedded. For defect interpolation, the arbitrarily shaped segment is formed by a local image region with defects, thus turning extrapolation into defect interpolation. Our algorithm reconstructs both oriented structures and noise-like information in a natural-looking manner, even for large defects. Moreover, our concept can also be applied to non-binary defect windows, e.g. for gain correction.

Keywords: Flat panel X-ray detectors, defect interpolation, spectral deconvolution, object-oriented transform coding

1. INTRODUCTION

Digital radiography has started to undergo profound changes with the advent of large flat panel detector systems.[1,2] Such electronic detector systems are, for instance, based on charge coupled devices (CCDs), which are optically coupled to an x-ray sensitive screen by fibers or lenses.[3] An alternative design uses a selenium panel which is charged homogeneously by a bias voltage before exposure to x radiation.[2] Yet another detector system which has been developed from flat panel display technology consists of a large array of light sensitive pixels that is manufactured from amorphous silicon (a-Si).[1,4,5] Sensitivity to x radiation is achieved by a coating of thallium-doped cesium-iodide (CsI:Tl). Advantages of electronic flat panel detectors over conventional radiography include the almost immediate availability of the acquired radiographs for viewing, the elimination of film costs, the possibility to digitally compensate over- or underexposure within certain limits, and the possibility of enhancement by digital filtering.[1,6,7] Moreover, a-Si flat panel detectors[1,4] also allow x-ray fluoroscopic imaging. Compared to current fluoroscopy detection front ends that consist of an image intensifier (II) optically coupled to a camera,[1,8] a flat detector is less bulky and avoids the geometric distortions caused by the generally convex entrance screen of the II. Furthermore, a flat panel detector is free of distortions which are caused by scattering in the II, like veiling glare.

Practically, large area flat solid state detectors contain inactive pixels (see e.g. Ref. 2, p. 287). Usually, the inactive pixels are known from calibration measurements. Defects in the acquired images can then be filled from adjacent pixels by suitable interpolation. The simplest approach is nonadaptive linear interpolation. A better reconstruction of orientated structures crossing a defect, like bone edges or catheters, is possible by nonlinear interpolation, for instance by a median filter,[2] or adaptive linear interpolation.[9] These interpolation algorithms work directly in the spatial domain, and generally give satisfactory results for defects that are sufficiently small. Since spatial domain interpolation includes weighted averaging of grey levels surrounding a defect, interpolated defects exhibit a different noise structure which may give the radiograph a somewhat unnatural appearance.

In this paper, we therefore describe an alternative interpolation algorithm that works in the spectral domain, and which is able to cope with both large defect areas and noise-like structures. Towards this end, the acquired distorted radiograph is modelled as the undistorted image multiplied by a known binary defect window. The effect of the

E-mail: aach@isip.mu-luebeck.de

defect window is then removed in the Fourier domain by deconvolving the window spectrum from the spectrum of the observed radiograph. In the spatial domain, the deconvolution corresponds to an extrapolation of the observed signal over the area where the binary window is zero. From the point of view of spectral analysis, deconvolution is equivalent to eliminating the smearing influence of the window spectrum. If successful, this permits the calculation of a higher resolved spectrum from the observed signal than allowed by the uncertainty relation.

Similar deconvolution problems arise in object oriented image analysis or coding, when the spectrum of a signal is needed which can only be observed inside a segment of arbitrary shape.[10–12] In the simplest case, the segment is zero-padded and embedded in a rectangle before applying a binary window which is one inside the segment, and zero outside. Both spectral feature extraction and efficient transform coding require that the window spectrum be removed.[13,14]

In the following, we first review approaches to the spectral analysis of windowed discrete signals. We then describe our interpolation algorithm, and show a number of results for synthetic as well as clinical data before concluding with a discussion.

2. SPECTRAL ANALYSIS, EXTRAPOLATION, AND SEGMENT CODING

For simplicity of notation, we consider a univariate discrete signal $f(n)$ of length N. Only a portion $g(n)$ of $f(n)$ can be observed inside a binary window $w(n)$, i.e. $g(n) = f(n) \cdot w(n)$, where $g(n)$ and $w(n)$ are also of length N. Convolution of the sought but unobservable spectrum of $f(n)$ with the window spectrum generates the spectrum $G(k)$ of the windowed observation $g(n)$, where the dominant spectral lines of $F(k)$ are smeared out. Estimation of the discrete Fourier spectrum $F(k)$ of $f(n)$ for $0 \leq k < N$ then consists of identifying the significant spectral lines of $f(n)$, and estimating their complex values. The iterative algorithm for bandlimited extrapolation in Ref. 15 assumes that the spectrum of $f(n)$ is limited to a known frequency band. Due to the window $w(n)$, the spectrum $G(k)$ of $g(n)$ exhibits contributions outside the known frequency band, which are set to zero, yielding a first spectral estimate $\hat{F}^{(1)}(k)$. Applying an inverse Fourier transform to $\hat{F}^{(1)}(k)$ yields a first extrapolated signal $\hat{f}^{(1)}(n)$. Due to the bandpass filtering, $\hat{f}^{(1)}(n)$ generally differs from the observed samples $g(n)$ of $f(n)$. Therefore, the samples of $\hat{f}^{(1)}(n)$ are replaced by the known samples inside the window $w(n)$. The resulting composite signal $c^{(1)}(n) = g(n) + (1 - w(n)) \cdot \hat{f}^{(1)}(n)$ then again exhibits spectral contributions outside the known frequency band, which in turn are eliminated by bandpass filtering. The iteration is continued until a sufficiently accurate estimate $\hat{F}^{(i)}(k)$ is reached. The algorithm is illustrated in Fig. 1. In Ref. 16, the algorithm is extended by an adaptive bandpass filter which selects only those in-band coefficients whose magnitude exceeds an adaptive threshold. The iterations can be viewed as alternating projections onto convex sets in spatial and Fourier domain, and convergence thus be proven. Obviously, each iteration of the extrapolation procedure requires a forward and an inverse DFT. One-step solutions to bandlimited extrapolation can be found in Refs. 17,18.

From the point of view of "good" extrapolation, the assumption of band limitation is often disadvantageous because it leads to extrapolations which rapidly decay outside the known observation interval. With respect to object oriented coding, these algorithms lack a selection and estimation strategy which is optimal in the sense of generating only a minimum number of nonzero frequency coefficients for a given reconstruction quality of $f(n)$ as evaluated inside the known observation interval. The latter issue is addressed by the "selective deconvolution" methods in Refs. 19,20, where the bandpass filtering in Fig. 1 is replaced by a selection of dominant conjugated spectral line pairs and optimal estimation of their complex values. The selective deconvolution algorithm also generates "good" extrapolations both for univariate signals and 2D image segments. Like Ref. 15, selective deconvolution is iterative and requires a forward and an inverse DFT per step.

An algorithm for spectral analysis and extrapolation which works completely in the Fourier domain was derived in Ref. 12, starting from ideas of selective deconvolution in Refs. 19,20. It combines optimal selection and estimation of DFT line pairs, and needs only one foward DFT at the beginning of the iteration, and an inverse DFT when it ends.

The discussed approaches to spectral analysis and extrapolation employ the discrete Fourier transform, and rely on the convolution theorem. In object oriented image coding, it is often desired to use other transforms like the discrete cosine transform (DCT). A DCT-based approach to segment oriented image coding can be found in Ref. 21. With respect to extrapolation, this algorithm is afflicted with the drawback of favouring lowpass-like extrapolations.

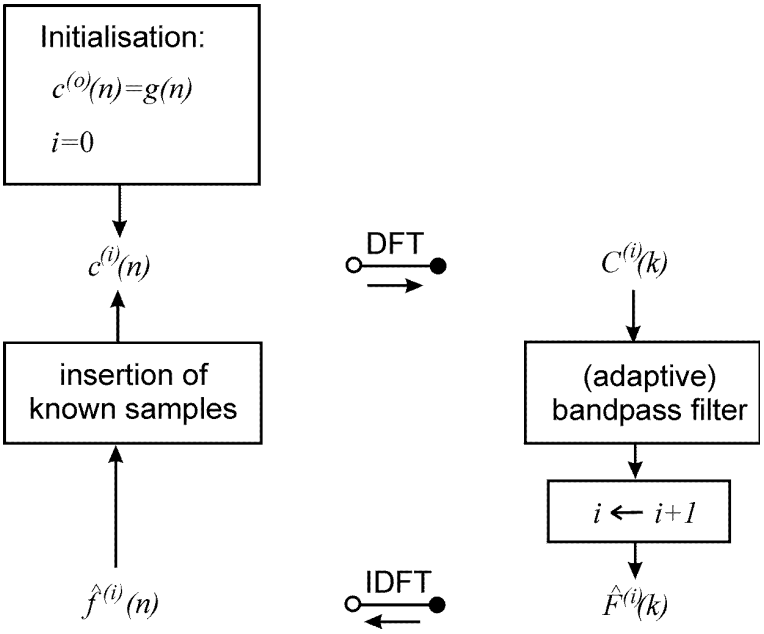

Figure 1. Illustration of the recursive algorithms for bandlimited spectral analysis in Refs. 15,16.

In Refs. 11,10, extrapolation and spectral analysis is approached from the point of view of linear approximation. A special framework — termed successive approximation — is developed which combines optimal approximation of the observed signal with estimation of its unknown values outside the observation window. The framework works with any orthogonal transform, including the DFT, the DCT, the Walsh transform and the discrete Hartley transform. The algorithms provide transform representations for efficient transform coding as well as generally good extrapolations. When the DFT is used, Ref. 10 boils down to the Fourier domain deconvolution of Ref. 12 discussed above, and which we use as a main ingredient of our extrapolation algorithm.

3. DEFECT INTERPOLATION BY SPECTRAL DECONVOLUTION

3.1. The Interpolation Algorithm

For notational convenience, we start with a univariate analysis. We model the observed signal $g(n)$ as

$$g(n) = f(n) \cdot w(n) \circ\!\!-\!\!\bullet\, G(k) = \frac{1}{N} F(k) * W(k) = \frac{1}{N} \sum_{l=0}^{N-1} F(l) \cdot W(k-l), \quad 0 \le n,k < N \tag{1}$$

where $f(n)$ is the undistorted signal, and $w(n)$ a binary defect window, with $w(n) = 1$ for $L < N$ samples, and $w(n) = 0$ if pixel n is inactive. $G(k)$, $F(k)$ and $W(k)$ are the DFT spectra of $g(n)$, $f(n)$ and $w(n)$, respectively. Both $f(n)$ and $g(n)$ are real valued, hence, $G(k) = G^*(N-k)$ and $F(k) = F^*(N-k)$. Our goal is to estimate $F(k) \bullet\!\!-\!\!\circ f(n)$ for $0 \le n,k < N$. Let us select a spectral line pair $G(s)$ and $G(N-s)$ of $G(k)$. If $F(k)$ consisted only of two lines at s and $N-s$, i.e.

$$F(k) = \hat{F}(k) = \hat{F}(s)\delta(k-s) + \hat{F}(N-s)\delta(k-N+s) \tag{2}$$

convolution with the window spectrum $W(k)$ would yield for the observed pair

$$\begin{aligned} G(s) &= \tfrac{1}{N}\Big(\hat{F}(s)\cdot W(0) + \hat{F}^*(s)\cdot W(2s)\Big) \\ G^*(s) &= \tfrac{1}{N}\Big(\hat{F}^*(s)\cdot W^*(0) + \hat{F}(s)\cdot W^*(2s)\Big) \end{aligned} \tag{3}$$

where $\hat{F}(s)$ and $\hat{F}(N-s) = \hat{F}^*(s)$ are the estimated coefficients. From (3), $\hat{F}(s)$ can be found to

$$\hat{F}(s) = N \cdot \frac{\big(G(s)W(0) - G^*(s)W(2s)\big)}{\big(|W(0)|^2 - |W(2s)|^2\big)} \tag{4}$$

The estimated spectrum $\hat{F}(k)$ would then be given by (2). Generally, $F(k)$ consists of more than two spectral lines. The error after deconvolution (4) at s and $N-s$ in the spectral domain is given by

$$G^{(1)}(k) = G(k) - \frac{1}{N} \cdot \hat{F}(k) * W(k) = G(k) - \frac{1}{N}\Big(\hat{F}(s) \cdot W(k-s) + \hat{F}^*(s) \cdot W(k+s)\Big) \tag{5}$$

$G^{(1)}(k)$ is the spectrum of the window internal difference signal

$$g^{(1)}(n) = g(n) - \hat{f}(n) \cdot w(n) = w(n)\big(f(n) - \hat{f}(n)\big) \tag{6}$$

Clearly, $G^{(1)}(k) = 0$ for $k = s$ and $k = N - s$.

Given s and $N-s$, the estimates $\hat{F}(s)$ and $\hat{F}(N-s)$ are optimal in the minimum mean square error (MMSE) sense if the energy E_g of $g^{(1)}(n)$ is minimized. Using Parseval's theorem, E_g can directly be evaluated in the spectral domain according to

$$E_g = \sum_{n=0}^{N-1}\Big(g^{(1)}(n)\Big)^2 = \frac{1}{N}\sum_{k=0}^{N-1}|G^{(1)}(k)|^2 = \frac{1}{N}\cdot E_G \tag{7}$$

In the appendix, it is shown that (4) indeed provides MMSE estimates for the sought frequency coefficients.

If the selected line pair $\hat{F}(s)$ and $\hat{F}(N-s)$ is dominant in a sense specified below, its convolution with $W(k)$ tends to "hide" other, less dominant spectral coefficients of $F(k)$. This influence is removed by (5), so that another line pair can be selected from $G^{(1)}(k)$, estimated and subtracted. This leads to the following iteration for spectral deconvolution:

- Initialization: $\hat{F}^{(0)}(k) = 0$, $G^{(0)}(k) = G(k)$, $i = 1$.
- i-th iteration step: Select a pair of spectral coefficients $G^{(i-1)}(s^{(i)})$, $G^{(i-1)}(N - s^{(i)})$ out of $G^{(i-1)}(k)$.
- Estimate $\hat{F}(s^{(i)})$, $\hat{F}(N - s^{(i)})$ according to (4) such that $G^{(i)}(s^{(i)}) = G^{(i)}(N - s^{(i)}) = 0$, i.e.

$$\begin{aligned} G^{(i-1)}(s^{(i)}) &= \tfrac{1}{N}\big(\hat{F}(s^{(i)})W(0) + \hat{F}^*(s^{(i)})W(2s^{(i)})\big) \\ \big(G^{(i-1)}(s^{(i)})\big)^* &= \tfrac{1}{N}\big(\hat{F}^*(s^{(i)})W(0) + \hat{F}(s^{(i)})W^*(2s^{(i)})\big) \end{aligned} \tag{8}$$

$$\Rightarrow \hat{F}(s^{(i)}) = N\Big(G^{(i-1)}(s^{(i)})W(0) - \big(G^{(i-1)}(s^{(i)})\big)^* W(2s^{(i)})\Big)\big/\big(|W(0)|^2 - |W(2s^{(i)})|^2\big)| \tag{9}$$

- Accumulation: Form the i-th estimate of $F(k)$ by the update $\hat{F}^{(i)}(k) = \hat{F}^{(i-1)}(k) + F_\Delta^{(i)}(k)$, with (see (2)) $F_\Delta^{(i)}(k) = \hat{F}(s^{(i)})\delta(k - s^{(i)}) + \hat{F}^*(s^{(i)})\delta\big(k - (N - s^{(i)})\big)$.
- End this step by forming the new error spectrum $G^{(i)}(k) = G^{(i-1)}(k) - \frac{1}{N}F_\Delta^{(i)}(k) * W(k)$.
- Start step $i+1$ by selecting a new line pair of $G^{(i)}(k)$.

Since we seek to minimize the error (7), the line pair we should select in the ith iteration is the one which maximizes the energy reduction $\Delta_E(\hat{F}(s^{(i)}))$, which can be calculated to (see (5) and (24) in the appendix)

$$\Delta_E\big(\hat{F}(s^{(i)})\big) = \frac{1}{N^2}\sum_{k=0}^{N-1}|\hat{F}(s^{(i)})W(k - s^{(i)}) + \hat{F}^*(s^{(i)})W(k + s^{(i)})|^2 \tag{10}$$

what can be rewritten to

$$\begin{aligned} \Delta_E \;=\; & \frac{1}{N^2}\hat{F}^*(s^{(i)}) \quad \textstyle\sum_{k=0}^{N-1}\Big[\hat{F}(s^{(i)})\,|W(k+s^{(i)})|^2 + \hat{F}^*(s^{(i)})W(k+s^{(i)})W^*(k-s^{(i)})\Big] \\ + \; & \frac{1}{N^2}\hat{F}(s^{(i)}) \quad \textstyle\sum_{k=0}^{N-1}\Big[\hat{F}^*(s^{(i)})\,|W(k-s^{(i)})|^2 + \hat{F}(s^{(i)})W(k-s^{(i)})W^*(k+s^{(i)})\Big] \end{aligned} \tag{11}$$

For a binary window, we have $w^2(n) = w(n)$. Inserting this into Parseval's theorem, we obtain

$$\begin{gathered}\sum_{k=0}^{N-1} |W(k+s^{(i)})|^2 = \sum_{k=0}^{N-1} |W(k-s^{(i)})|^2 = \sum_{k=0}^{N-1} |W(k)|^2 = N \sum_{n=0}^{N-1} w(n) = N \cdot W(0) \\ \sum_{k=0}^{N-1} W(k+s^{(i)}) W^*(k-s^{(i)}) = N \sum_{n=0}^{N-1} w(n) \exp\{-j2\pi \tfrac{2s^{(i)}}{N} n\} = N \cdot W(2s^{(i)}) \end{gathered} \tag{12}$$

Inserting (12) into (11) yields

$$\Delta_E = \hat{F}^*(s^{(i)}) \cdot G^{(i-1)}(s^{(i)}) + \hat{F}(s^{(i)}) \cdot \left(G^{(i-1)}(s^{(i)})\right)^* \tag{13}$$

Since we know how to estimate $\hat{F}(s^{(i)})$ optimally (9), $\hat{F}^*(s^{(i)})$ can be eliminated, thus expressing the error energy reduction depending on the available error spectrum line $G^{(i-1)}(k_s^{(i)})$ as

$$\Delta_E = N \cdot \frac{2\,|G^{(i-1)}(s^{(i)})|^2\, W(0) - 2Re\left\{\left(G^{(i-1)}(s^{(i)})\right)^2 \cdot W^*(2s^{(i)})\right\}}{|W(0)|^2 - |W(2s^{(i)})|^2} \tag{14}$$

Selecting the best line pair in each iteration hence implies finding s such that Δ_E according to (14) is maximum. Because of the symmetry of the DFT spectra of real valued signals, it suffices to search over only half the coefficients of $G^{(i-1)}(k)$, i.e. from $k = 0$ to $k = N/2$, to find $s^{(i)}$.

Let us also mention here that for $s^{(i)} = 0$ and $s^{(i)} = N/2$, i.e. the DC-coefficient and the coefficient representing the highest possible frequency, no conjugate lines exist. We can the only select the single lines $G^{(i-1)}(0)$ or $G^{(i-1)}(N/2)$ rather than line pairs. As shown in the appendix, the estimation according to (9) of $\hat{F}^*(s^{(i)})$, $s^{(i)} = 0$ or $s^{(i)} = N/2$ then simplifies to

$$\hat{F}(s^{(i)}) = \frac{N}{W(0)} \cdot G^{(i-1)}(s^{(i)}) \tag{15}$$

Similarly, the calculation of the error energy reduction Δ_E according to (14) modifies to

$$\Delta_E = \frac{2N}{W(0)} \cdot |G^{(i-1)}(s^{(i)})|^2 \tag{16}$$

Clearly, when selecting only a single line, the error energy reduction depends only on the modulus spectrum $|G^{(i-1)}(s^{(i)})|$, apart from a constant factor. To save computational expense in the selection step, a simplified approach is to always select $s^{(i)}$ such that $|G^{(i-1)}(s^{(i)})|$ is maximum, regardless of whether a single line is tested, that is, $s^{(i)} = 0$ or $s^{(i)} = N/2$, or a line pair. Practically, the outcome of the iteration remains almost unchanged.

When the estimated spectrum $\hat{F}^*(s^{(i)})$ contains as many lines as there are samples of $f(n)$ inside the window $w(n)$, the remaining error energy E_G vanishes. The backtransformed estimate $\hat{f}^{(i)}(n)$ is then identical to $g(n)$ inside the observation window, and contains extrapolated information outside. In practice, the iteration is stopped when Δ_E falls below a prespecified level ϵ, or when a maximum number of iterations is reached.

To achieve high spectral resolution for the interpolated signal, it is often reasonable to apply zero-padding to $g(n)$ and $w(n)$ before transforming and starting the iteration. An illustration of the entire recursion is given in Fig. 2.

3.2. Implementation using the FFT

Let us briefly discuss the 2D-implementation of our algorithm. Without loss of generality, let us assume the defect to be embedded in a rectangle of size $N \times N$ pixels. We then observe

$$g(m,n) = f(m,n) \cdot w(m,n) \circ\!\!-\!\!\bullet\, G(k,l) = \frac{1}{N^2} F(k,l) * W(k,l)\ , \quad 0 \le m,n,k,l < N \tag{17}$$

When selecting and estimating a coefficient at (s,t), conjugated line pairs can be considered except for $(s,t) = (0,0)$, $(s,t) = (0,N/2)$, $(s,t) = (N/2,0)$ and $(s,t) = (N/2,N/2)$, where only a single line can be selected. In the former case, (14) for the calculation of the reduction of the error energy and (9) for estimation straightforwardly extend to the bivariate case. In the latter, the bivariate equivalents of (16) and (15) apply. Obviously, because of the symmetry of the DFT-spectra, it suffices to search only one halfplane in the selection step. Let us finally mention that because of the implicit periodicity of the DFT, all arguments which may exceed N or be lower than zero must be evaluated modulo N. For instance, $2s$ would have to be evaluated as $(2s) \mathrm{mod} N$, etc.

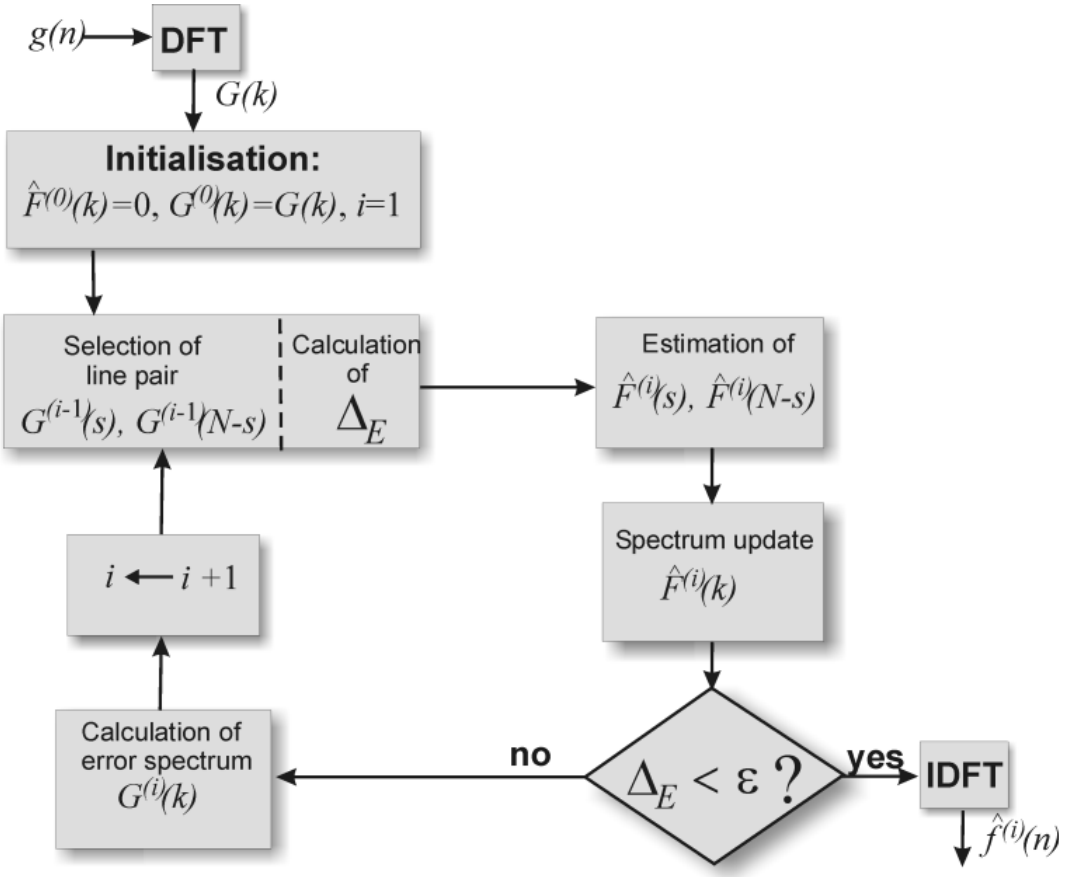

Figure 2. Illustration of the recursive spectral deconvolution algorithm. From the final spectral estimate $\hat{F}^{(i)}(k)$, the interpolated signal estimate is obtained by an inverse DFT. Unlike the algorithm in Fig. 1, only one spectral transform is required when starting or ending the iteration, but not two per step.

4. RESULTS

Fig. 3 shows application of our spectral defect interpolation algorithm to a textured image with a large defect of size 32×32 pixels. The restored image is shown in Fig. 3b). The estimation result was inserted into the defect, with the original outside the defect window. 100 iterations using the simplified selection by modulus coefficients were applied. Mathematically, the restoration $f_r(m,n)$ is then given by

$$f_r(m,n) = g(m,n) + (1 - w(m,n))\hat{f}^{(100)}(m,n) \tag{18}$$

Also depicted in Fig. 3c) is the error energy reduction Δ_E according to Eqs. (14) and (16), where the image size N was normalized out. Evidently, the extrapolation result fits well with the known samples, and is almost free of blurring.

To test the ability of our extrapolation algorithm to cope with noise without generating an unnatural appearance, we replaced the texture image by simulated white noise (Fig. 4). Processing parameters were the same as for Fig. 3, but the number of iterations was increased to 500. Clearly, our algorithm is able to cope with noise, and to extrapolate noise signals in a natural manner. This is remarkable since unlike the textured image, white noise by definition does not possess dominant spectral lines. The steep drop-off of the error enregy reduction over for the first iteration step is due to the fact that for purposes of visualization, a positive mean value was added to the originally zero-mean signal, which is estimated first.

Fig. 5 shows results for a radiograph of size 482×482 pixels, which is subjected to a synthetically generated defect map. For testing purposes, the depicted defects are larger and more numerous than in real detectors. The

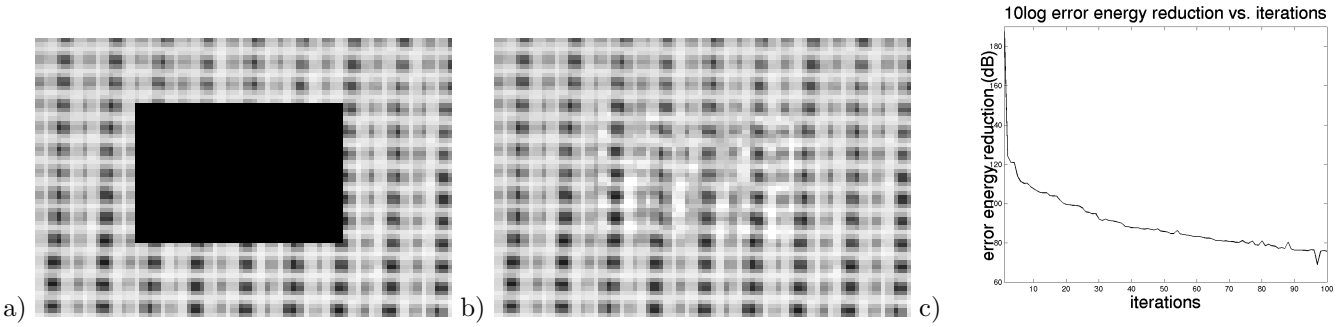

Figure 3. a) Textured image of size 64×64 pixels with a defect of size 32×32 pixels in its centre. b) Image a) with the restored defect inserted. c) Normalized spectral error energy reduction Δ_E/N over iterations.

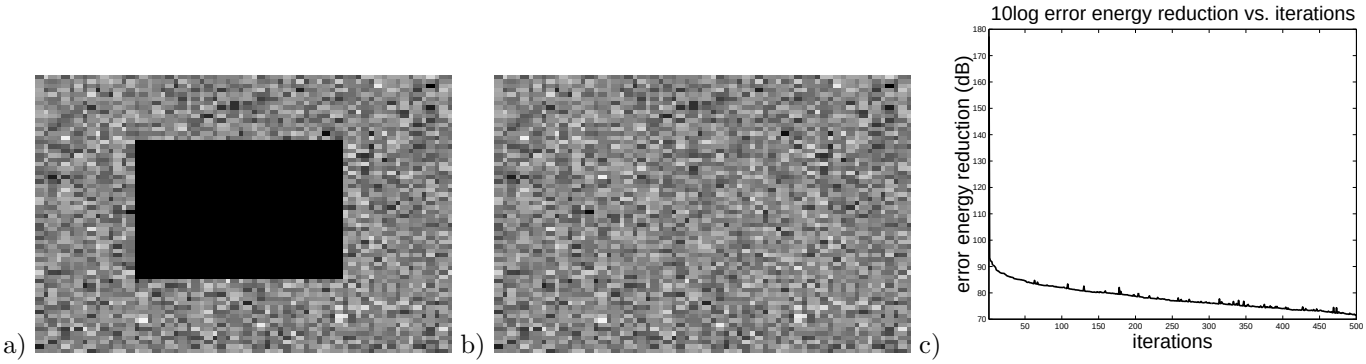

Figure 4. a) Simulated white noise image of size 64×64 pixels with a defect of size 32×32 pixels in its centre. b) Image a) with the restored defect inserted. c) Normalized spectral error energy reduction Δ_E/N over iterations.

defective image is shown in Fig. 5c), and the restored one in Fig. 5d). Enlarged detail areas are shown in Fig. 6. While one would usually limit the algorithm to a rectangle embedding a large defect, we have here processed the entire image based on blocks of size 64×64 pixels, which overlapped by 32 pixels in each dimension. Each block was zero padded to 128×128 pixels. After each block was extrapolated, the extrapolation result from the central region, i.e. from $(17, 17)$ to $(48, 48)$ of each block was inserted into the defective image. The simplified selection procedure by the maximum modulus was used.

Results for another radiograph are given in Fig. 7. Processing parameters were identical to those in Fig. 5.

5. DISCUSSION AND CONCLUSIONS

As an alternative to spatial domain defect interpolation algorithms, we have in this paper described a spectral domain approach. While in the spatial domain defect generation can be modelled as multiplication of the undistorted image by a defect map, we have in the spectral domain a convolution between image spectrum and spectrum of the defect window. Defect interpolation then corresponds to a deconvolution of these spectra. We have shown that similar problems have been addressed in the area of transform-based segment oriented image coding.[10] Our approach is particularly suited to large defective areas or to cases where simple algorithms cause problems because of their explicit or implicit averaging. The good behaviour of our method was demonstrated both with texture signals containing dominant spatial frequencies and with noise-like signals with a spread-out spectrum. The price to pay is a relatively high computational complexity of our algorithm. Practically, one would therefore apply this algorithm to a few large defects only, where spatial domain interpolation fails. To reduce the number of iterations needed, one could replace the estimation of a line pair by simultaneously estimating all so far selected lines (successive best-approximation[10,12]). This limits the theoretical maximum number of iterations to obtain a vanishing error energy to about half the number of observed samples. However, each iteration step then becomes computationally more expensive. Another possibility to reduce the number of iterations is to first apply a spatial interpolation algorithm, and to initialize $\hat{F}^{(0)}(k)$ in Fig. 2 by the DFT spectrum of the interpolation result of this algorithm. Since this is generally a much better initial estimate than the empty defect, less iterations should be required to reach an artifact-free final interpolation.

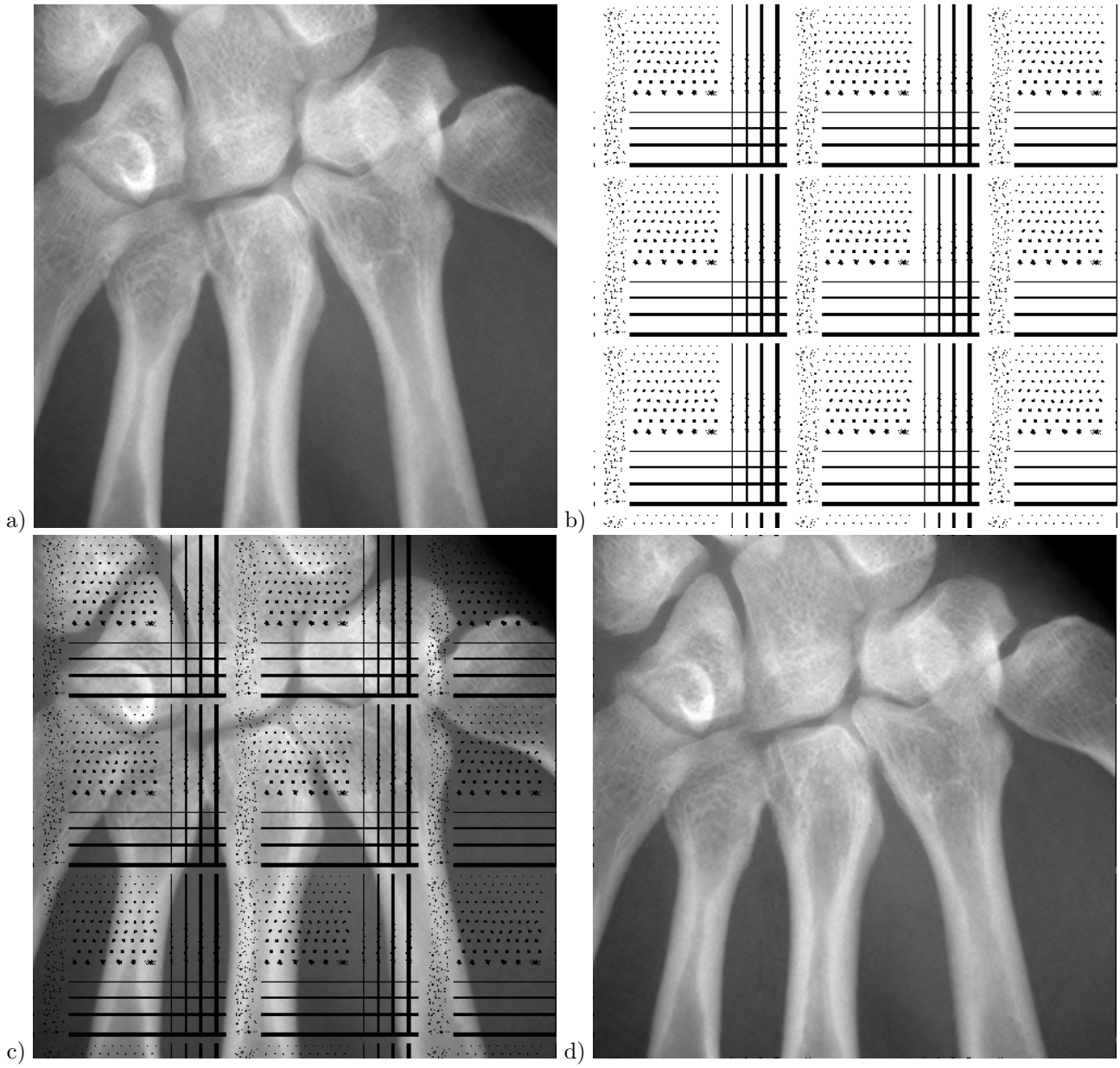

Figure 5. a) Example part of a radiograph of size 482×482 pixels, b) synthetic defect map (exaggerated), where inactive pixels are black, c) simulated defective acquired radiograph, d) defective radiograph after spectral restoration.

a) 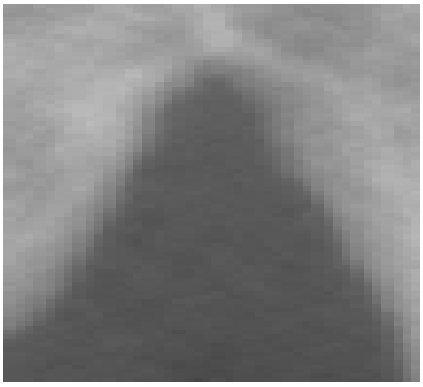 b) 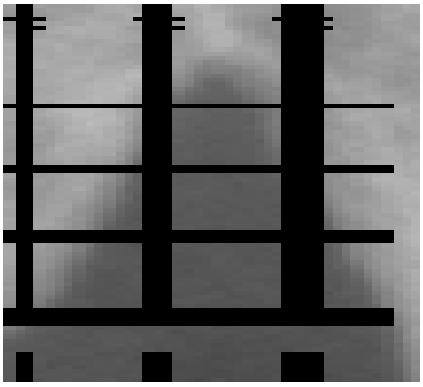 c) 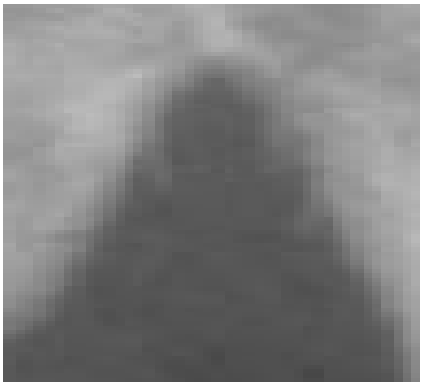

Figure 6. Detail area from (140,233) to (181,319) from Fig. 5 for a) the original, b) the defective image and c) the restored image.

Another advantage of our algorithm is that it can be extended to non-binary windows, i.e. to cases where pixels are not equally sensitive but still active. For such gain correction, the assumption $w^2(n) = w(n)$ would have to be dropped. Still, equations for line selection and estimation can be derived.

6. APPENDIX

We first indirectly prove that, given s and $N-s$, the error energy E_G is minimized by estimating $F(s)$ and $F(N-s) = F^*(s)$ as given in (4). To this end, we consider another estimate $\tilde{F}(s) = \hat{F}(s) + a$, which differs from $\hat{F}(s)$ by a, where a is complex. The error spectrum then evaluates to

$$\tilde{G}^{(1)}(k) = G(k) - \frac{1}{N}\left(\tilde{F}(s)\cdot W(k-s) + \tilde{F}^*(s)\cdot W(k+s)\right) = G^{(1)}(k) - D(k) \tag{19}$$

where $D(k) = (1/N)\big(aW(k-s) + a^*W(k+s)\big)$. The difference $\Delta_E(a)$ between the energy $\tilde{E}_G$ of $\tilde{G}^{(1)}(k)$ and E_G in (5) is given by

$$\Delta_E(a) = \tilde{E}_G - E_G = \sum_{k=0}^{N-1}|D(k)|^2 - \sum_{k=0}^{N-1}\big(G^{(1)}(k)\big)^* D(k) - \sum_{k=0}^{N-1} G^{(1)}(k)D^*(k) \tag{20}$$

and can be rewritten to

$$\Delta_E(a) = \sum_{k=0}^{N-1}|D(k)|^2 - \frac{2}{N}\mathrm{Re}\left[a^*\sum_{k=0}^{N-1}G^{(1)}(k)W^*(k-s) + a\sum_{k=0}^{N-1}G^{(1)}(k)W^*(k+s)\right] \tag{21}$$

With $\sum_k S_1(k)\cdot S_2^*(k) = N\cdot\sum_n s_1(n)\cdot s_2^*(n)$, we have

$$\begin{aligned}\Delta_E(a) = \sum_{k=0}^{N-1}|D(k)|^2 \quad -2\mathrm{Re}\Bigg[a^*\textstyle\sum_{n=0}^{N-1} g^{(1)}(n)\Big(w(n)\exp\big(j2\pi\frac{s}{N}n\big)\Big)^* \\ +a\textstyle\sum_{n=0}^{N-1} g^{(1)}(n)\Big(w(n)\exp\big(-j2\pi\frac{s}{N}n\big)\Big)^*\Bigg]\end{aligned} \tag{22}$$

Since $w(n)$ is a binary window, we have $w(n)g^{(1)}(n) = g^{(1)}(n)$, and thus

$$\begin{aligned}\Delta_E(a) = \quad & \textstyle\sum_{k=0}^{N-1}|D(k)|^2 - 2\Bigg[a^*\sum_{n=0}^{N-1} g^{(1)}(n)\exp\big(-j2\pi\frac{s}{N}n\big) + a\sum_{n=0}^{N-1} g^{(1)}(n)\exp\big(j2\pi\frac{s}{N}n\big)\Bigg] \\ = \quad & \textstyle\sum_{k=0}^{N-1}|D(k)|^2 - 2\big[a^*G^{(1)}(s) + aG^{(1)}(N-s)\big]\end{aligned} \tag{23}$$

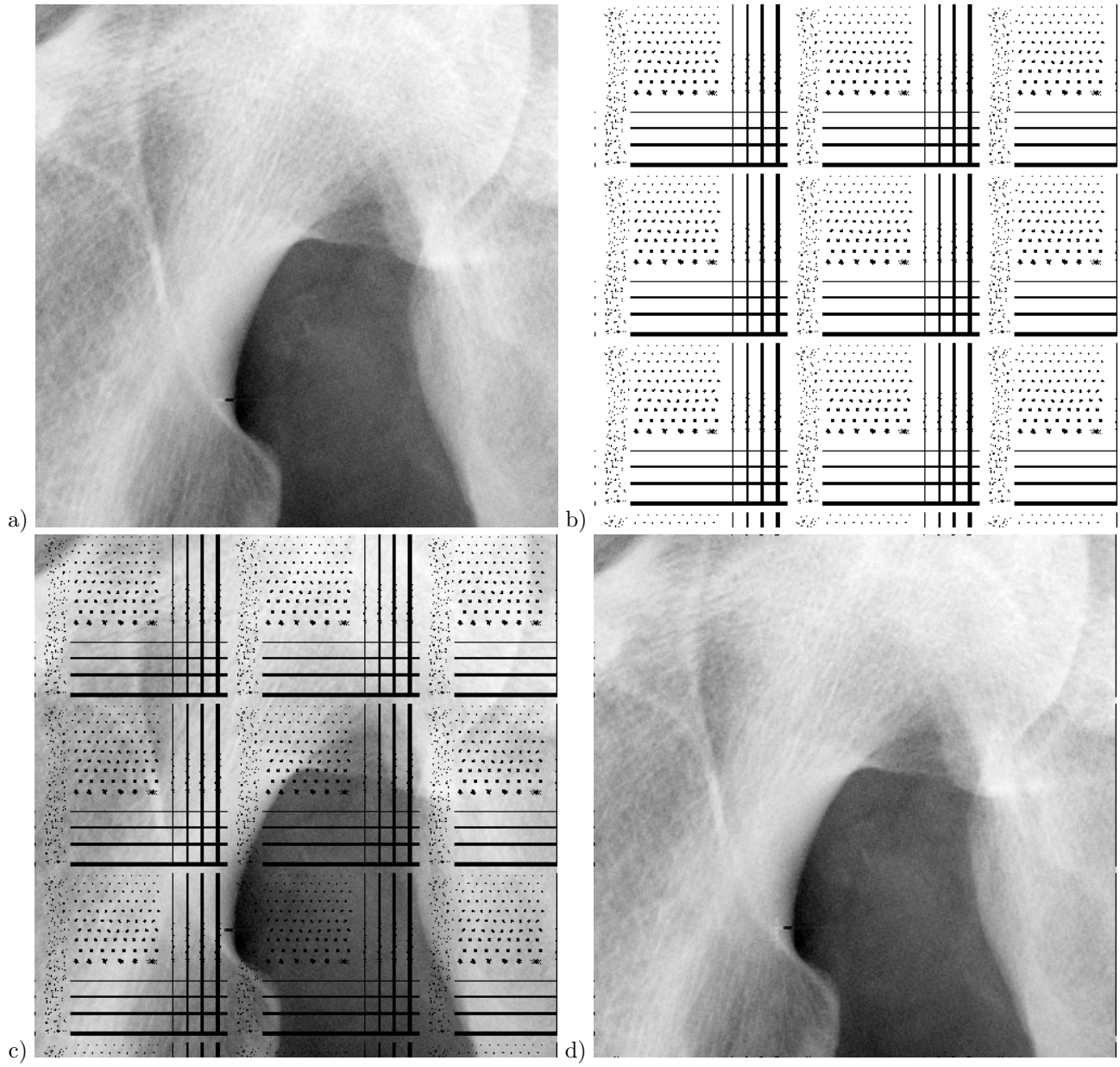

Figure 7. a) Example part of a radiograph of size 482×482 pixels, b) synthetic defect map (exaggerated), where inactive pixels are black, c) simulated defective acquired radiograph, d) defective radiograph after spectral restoration.

According to (4), $G^{(1)}(s) = G^{(1)}(N-s) = 0$, yielding

$$\Delta_E(a) = \frac{1}{N^2} \sum_{k=0}^{N-1} |aW(k-s) + a^* W(k+s)|^2 \tag{24}$$

which is greater than zero if $a \neq 0$. Hence, E_G is always smaller than $\tilde{E}_G$.

Rather than from the reasoning in the beginning of section 3, the equations (9) and (15) for estimating spectral lines can also be derived by calculating the derivative of the spectral error energy E_G with respect to the sought spectral lines. From (5) and (7), the error energy after the ith iteration step can expressed as

$$E_G = \sum_{k=0}^{N-1} |G^{(i)}(k)|^2 = \sum_{k=0}^{N-1} |G^{(i-1)}(k) - \frac{1}{N} \cdot \hat{F}_{\Delta}^{(i)}(k) * W(k)|^2 \tag{25}$$

Eq. (9) can then be obtained by partially differentiating E_G with respect to $\hat{F}^{(i)}(s)$ and $\hat{F}^{(i)}(N-s)$, and equating the derivatives to zero. Solving the resulting set of two equations for $\hat{F}^{(i)}(s)$ and $\hat{F}^{(i)}(N-s)$ yields (9). If a single line is $\hat{F}^{(i)}(s)$ is selected, deriving E_G with respect to $\hat{F}^{(i)}(s)$, equating to zero and solving for $\hat{F}^{(i)}(s)$ yields (15).

REFERENCES

1. T. Aach, U. Schiebel, and G. Spekowius, "Digital image acquisition and processing in medical x-ray imaging," *Journal of Electronic Imaging* **8**(Special Section on Biomedical Image Representation), pp. 7–22, 1999.
2. J. A. Rowlands and J. Yorkston, "Flat panel detectors for digital radiography," in *Handbook of Medical Imaging*, J. Beutel, H. L. Kundel, and R. L. van Metter, eds., pp. 223–328, Springer Verlag, 2000.
3. R. Guillemaud and L. Simon, "Evaluation of a fluoroscopy mode for a CCD-based radiographic detector," in *Medical Imaging 2000: Physics of Medical Imaging*, J. Dobbins and J. Boone, eds., pp. 137–144, SPIE Volume 3977, (Bellingham, Washington), February 2000.
4. N. Jung, P. L. Alving, F. Busse, N. Conrads, H. M. Meulenbrugge, W. Rütten, U. Schiebel, M. Weibrecht, and H. Wieczorek, "Dynamic x-ray imaging system based on an amorphous silicon thin-film array," in *Physics of Medical Imaging*, vol. SPIE Vol. 3336, 1998.
5. T. C. J. Bruijns, T. Adraansz, A. R. Cowen, A. G. Davies, S. M. Kengyelics, K. Kiani, H. Kroon, and H. Luijendijk, "Simulation of the quality of an a-Si flat x-ray detector system in low dose fluoroscopic applications," in *Medical Imaging 2000: Physics of medical Imaging*, J. Dobbins and J. Boone, eds., pp. 117–127, SPIE Volume 3977, (Bellingham, Washington), February 2000.
6. M. Stahl, T. Aach, S. Dippel, T. Buzug, R. Wiemker, and U. Neitzel, "Noise-resistant weak-structure enhancement for digital radiography," in *SPIE Medical Imaging 99: Image Processing*, K. M. Hanson, ed., pp. 1406–1417, SPIE Vol. 3661, (San Diego, USA), February 20–26 1999.
7. M. Stahl, T. Aach, and S. Dippel, "Digital radiography enhancement by nonlinear multiscale processing," *Medical Physics* **27**(1), pp. 56–65, 2000.
8. G. Spekowius, H. Boerner, W. Eckenbach, P. Quadflieg, and G. J. Laurenssen, "Simulation of the imaging performance of x-ray image intensifier/ TV camera chains," in *Medical Imaging 1995*, pp. 12–23, (SPIE Vol. 2432), 1995.
9. F. Xu, H. Liu, G. Wang, and B. A. Alford, "Comparison of adaptive linear interpolation and conventional linear interpolation for digital radiography systems," *Journal of Electronic Imaging* **9**(1), pp. 22–31, 2000.
10. A. Kaup and T. Aach, "Coding of segmented images using shape-independent basis functions," *IEEE Transactions on Image Processing* **7**(7), pp. 937–947, 1998.
11. A. Kaup and T. Aach, "A new approach towards description of arbitrarily shaped image segments," in *Proceedings International Workshop on Intelligent Signal Processing and Communication Systems*, pp. 543–553, IEEE, (Taipei, Taiwan), Mar 1992.
12. R. Sottek, K. Illgner, and T. Aach, "An efficient approach to extrapolation and spectral analysis of discrete signals," in *Informatik Fachberichte 253*, W. Ameling, ed., pp. 103–108, ASST 90, Springer Verlag, (Aachen, FRG), September 1990.

13. S. F. Chang and D. G. Messerschmitt, "Comparison of transform coding techniques for two-dimensional arbitrarily-shaped images," *ACM/Springer International Journal of Multimedia Systems* **1**(6), pp. 231–239, 1994.
14. W. Philips, "A comparison of four hybrid block/object image coders," *Signal Processing* **54**, pp. 103–107, 1996.
15. A. Papoulis, "A new algorithm in spectral analysis and band-limited extrapolation," *IEEE Transactions on Circuits and Systems* **CAS-22**(9), pp. 735–742, 1975.
16. A. Papoulis, "Detection of hidden periodicities by adaptive extrapolation," *IEEE Transactions on Acoustics, Speech, and Signal Processing* **ASSP-27**(1), pp. 4–12, 1979.
17. M. S. Sabri and W. S. Steenart, "An approach to band-limited extrapolation: The extrapolation matrix," *IEEE Transactions on Circuits and Systems* **CAS-25**(2), pp. 74–78, 1978.
18. J. A. Cadzow, "An extrapolation procedure for band-limited signals," *IEEE Transactions on Acoustics, Speech, and Signal Processing* **ASSP-27**(5), pp. 492–500, 1979.
19. U. Franke, "Selective deconvolution: A new approach to extrapolation and spectral analysis of discrete signals," in *Proceedings International Conference on Acoustics, Speech, and Signal Processing (ICASSP)*, pp. 1300–1303, IEEE, (Dallas), 1987.
20. U. Franke and R. Mester, "Region based image representation with variable reconstruction quality," in *Proceedings Visual Communications and Image Processing (SPIE Vol. 1001)*, pp. 178–186, SPIE, (Cambridge, Mass.), November 1988.
21. H. H. Chen, M. R. Civanlar, and B. G. Haskell, "A block transform coder for arbitrariliy shaped image segments," in *Proceedings IEEE International Conference on Image Processing (ICIP)*, pp. 85–89, IEEE, (Austin, TX), November 1994.